

## Stereomutation of Pentavalent Compounds: Validating the Berry Pseudorotation, Redressing Ugi's Turnstile Rotation, and Revealing the Two- and Three-Arm Turnstiles

Erik P. A. Couzijn,<sup>\*,†,‡</sup> J. Chris Slootweg,<sup>†</sup> Andreas W. Ehlers,<sup>†</sup> and Koop Lammertsma<sup>\*,†</sup>

Department of Chemistry and Pharmaceutical Sciences, Faculty of Sciences, VU University Amsterdam, De Boelelaan 1083, 1081 HV Amsterdam, The Netherlands, and Laboratorium für Organische Chemie, ETH Zürich, Wolfgang-Pauli-strasse 10, CH-8093 Zürich, Switzerland

Received June 17, 2010; E-mail: couzijn@org.chem.ethz.ch; k.lammertsma@few.vu.nl

© This paper contains enhanced objects available on the Internet at <http://pubs.acs.org/jacs>.

**Abstract:** A general reaction mechanism describes the qualitative change in chemical topology along the reaction pathway. On the basis of this principle, we present a method to characterize intramolecular substituent permutation in pentavalent compounds. A full description of the geometry around five-coordinate atoms using internal coordinates enables the analysis of the structural changes along the stereomutational intrinsic reaction coordinate. The fluxional behavior of experimentally known pentavalent phosphoranes, silicates, and transition-metal complexes has been investigated by density functional theory calculations, and three principal mechanisms have been identified: Berry pseudorotation, threefold cyclic permutation, and half-twist axial-equatorial interchange. The frequently cited turnstile rotation is shown to be equivalent to the Berry pseudorotation. In combination with graph theory, this approach provides a means to systematically investigate the stereomutation of pentavalent molecules and potentially identify hitherto-unknown mechanisms.

### Introduction

Conformational flexibility in pentavalent compounds<sup>1</sup> affects the stereoselectivity of many organic, inorganic, and organometallic reactions. Representative of this flexibility is the prototypical molecule PF<sub>5</sub> (**1**), whose structure is well-defined in the solid state<sup>2</sup> but dynamic in solution<sup>3</sup> with a permutational barrier of only 3.1 kcal mol<sup>-1</sup>.<sup>4</sup> The stereochemistry of nucleophilic substitution at silicon, for example, is dictated by the intermediacy of a fluxional silicate.<sup>5</sup> Such dynamic behavior is not unique to pentavalent main-group elements only. Illustrative is the enantioselective alkene metathesis based on the fluxionality of “stereogenic-at-Mo” alkylidene complexes,<sup>6</sup> whereas in the Rh-catalyzed olefin hydroformylation cycle, stereomutation may hamper asymmetric conversions.<sup>7,8</sup> Many more examples can be found in the literature. In addition, the principles

underlying the conformational nonrigidity have been amply addressed, resulting in the Berry pseudorotation<sup>9</sup> and the turnstile rotation<sup>10</sup> as common mechanisms in standard textbooks.<sup>11</sup> Such general reaction mechanisms qualitatively describe the changes

<sup>†</sup> VU University Amsterdam.

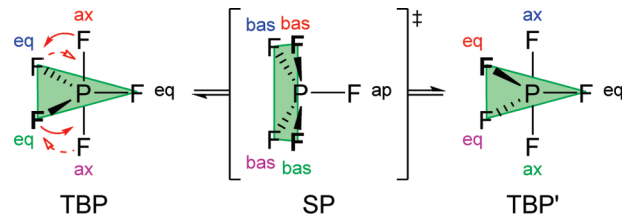
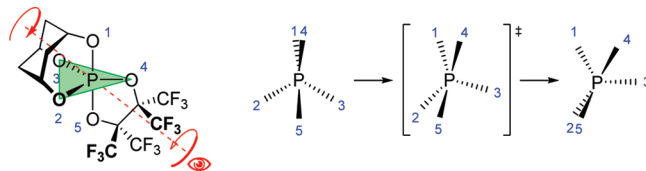
<sup>‡</sup> ETH Zürich.

- (1) Pentavalent compounds contain a five-coordinate atom without lone pairs. Pentacoordinate hexavalent centers are better described as octahedral with the lone pair as the sixth “substituent” and can stereoisomerize either by the hexavalent counterpart of 120° turnstile rotation via a trigonal prism or by inversion of the lone pair. See: Rzepa, H. S.; Cass, M. E. *Inorg. Chem.* **2006**, *45*, 3958–3963.
- (2) Mootz, D.; Wiebcke, M. Z. *Anorg. Allg. Chem.* **1987**, *545*, 39–42.
- (3) (a) Gutowsky, H. S.; Liehr, A. D. *J. Chem. Phys.* **1953**, *20*, 1652–1653. (b) Gutowsky, H. S.; McCall, D. W.; Slichter, C. P. *J. Chem. Phys.* **1953**, *21*, 279–292. (c) Maier, L.; Schmutzler, R. *Chem. Commun.* **1969**, 961–962.
- (4) (a) Bernstein, L. S.; Kim, J. J.; Pitzer, K. S.; Abramowitz, S.; Levin, I. W. *J. Chem. Phys.* **1975**, *62*, 3671–3675. (b) Bernstein, L. S.; Abramowitz, S.; Levin, I. W. *J. Chem. Phys.* **1976**, *64*, 3228–3236.
- (5) Review: Holmes, R. R. *Chem. Rev.* **1990**, *90*, 17–31.

- (6) (a) Marinescu, S. C.; Schrock, R. R.; Li, B.; Hoveyda, A. H. *J. Am. Chem. Soc.* **2009**, *131*, 58–59. (b) Malcolmson, S. J.; Meek, S. J.; Sattely, E. S.; Schrock, R. R.; Hoveyda, A. H. *Nature* **2008**, *456*, 933–937. (c) Sattely, E. S.; Meek, S. J.; Malcolmson, S. J.; Schrock, R. R.; Hoveyda, A. H. *J. Am. Chem. Soc.* **2009**, *131*, 943–953. (d) Klare, H. F. T.; Oestreich, M. *Angew. Chem., Int. Ed.* **2009**, *48*, 2085–2089.
- (7) (a) Brown, J. M.; Kent, A. G. *J. Chem. Soc., Perkin Trans. 2* **1987**, 1597–1607. (b) Buisman, G. J. H.; van der Veen, L. A.; Kamer, P. C. J.; van Leeuwen, P. W. N. M. *Organometallics* **1997**, *16*, 5681–5687. (c) van der Slot, S. C.; Kamer, P. C. J.; van Leeuwen, P. W. N. M.; Iggo, J. A.; Heaton, B. T. *Organometallics* **2001**, *20*, 430–441.
- (8) (a) Koga, N.; Jin, S. Q.; Morokuma, K. *J. Am. Chem. Soc.* **1988**, *110*, 3417–3425. (b) Matsubara, T.; Koga, N.; Ding, Y.; Musaev, D. G.; Morokuma, K. *Organometallics* **1997**, *16*, 1065–1078. (c) Decker, S. A.; Cundari, T. R. *Organometallics* **2001**, *20*, 2827–2841.
- (9) (a) Berry, R. S. *J. Chem. Phys.* **1960**, *32*, 933–938. (b) Berry, R. S. *Rev. Mod. Phys.* **1960**, *32*, 447–454.
- (10) (a) Ugi, I.; Marquarding, D.; Klusacek, H.; Gokel, G.; Gillespie, P. *Angew. Chem., Int. Ed. Engl.* **1970**, *9*, 703–730. (b) Gillespie, P.; Hoffman, P.; Klusacek, H.; Marquarding, D.; Pfohl, S.; Ramirez, F.; Tsolis, E. A.; Ugi, I. *Angew. Chem., Int. Ed. Engl.* **1971**, *10*, 687–715. (c) Ugi, I.; Marquarding, D.; Klusacek, H.; Gillespie, P. *Acc. Chem. Res.* **1971**, *4*, 288–296. (d) Ramirez, F.; Ugi, I.; Lin, F.; Pfohl, S.; Hoffman, P.; Marquarding, D. *Tetrahedron* **1974**, *30*, 371–376. (e) Ramirez, F.; Chaw, Y. F.; Marecek, J. F.; Ugi, I. *J. Am. Chem. Soc.* **1974**, *96*, 2429–2433.
- (11) Moss, G. P. *Pure Appl. Chem.* **1996**, *68*, 2193–2222. The IUPAC recommendations describe turnstile rotation as a 120° rotation of an *ax,eq* bond pair relative to the other three bonds, but the accompanying diagram shows a 60° rotation.

**Table 1.** Common Abbreviations Used in This Article

TBP	trigonal bipyramidal
<i>ax</i>	axial
<i>eq</i>	equatorial
SP	square pyramid
<i>ap</i>	apical
<i>bas</i>	basal
BPR	Berry pseudorotation
TR	turnstile rotation
TS	transition structure
IRC	intrinsic reaction coordinate
TP	topology parameter

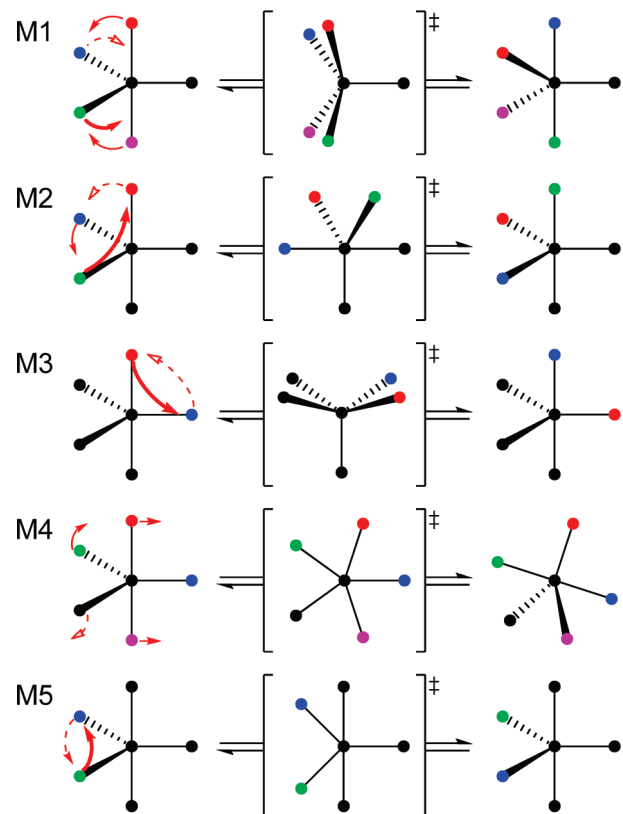
**Scheme 1.** Interconversion of Extreme Pentavalent Geometries via the Berry Pseudorotation (The Label Colors Distinguish the Permuting Substituents)**Scheme 2.** Turnstile Rotation of Oxyphosphorane **2** Viewed along the Approximate  $C_3/C_2$  Internal Rotation Axis

in chemical topology for compound-specific *physical* reaction mechanisms (i.e., exact atomic motions).<sup>12</sup> In this article, we show that adjustments in the accepted general stereomutation mechanisms are warranted.

Pentavalent species usually show a slight energetic preference for a trigonal bipyramidal (TBP) conformer with two axial (*ax*) and three equatorial (*eq*) groups over the square pyramid (SP) form that has one apical (*ap*) and four basal (*bas*) groups (see Table 1 for a list of abbreviations used in this article). The best-known interconversion, as illustrated for  $\text{PF}_5$  in Scheme 1, proceeds via the Berry pseudorotation (BPR),<sup>9</sup> in which the two *ax* substituents of the TBP conformer interchange with two *eq* groups by simultaneous contraction/expansion of the respective valence angles; the SP conformer is in this case the transition structure (TS). The other established stereomutation mechanism, the turnstile rotation (TR), was proposed by Ugi et al.<sup>10a,b</sup> on the basis of topology and group theory and is illustrated for caged oxyphosphorane **2** in Scheme 2. This mechanism divides the substituents into a trio and a pair that undergo a 60° relative rotation.<sup>10,11</sup> Notably, some have argued that the BPR and TR stereomutations are equivalent.<sup>13</sup>

Earlier, Muetterties derived *five* possible general permutation mechanisms on the basis of a topological analysis; these are

(12) We distinguish between a *physical* reaction mechanism, which applies to a specific system and can be described by the exact atomic displacements along the intrinsic reaction coordinate, and a *general* reaction mechanism, which relates the analogous behavior of various systems by describing the qualitative changes in chemical topology along their reaction pathways; also see ref 13a. This is discussed in further detail in section 1.1 of the Addendum in the Supporting Information.

**Scheme 3.** Possible General Stereomutation Mechanisms (Colored Dots Represent the Interchanging Groups)

displayed in Scheme 3.<sup>14</sup> Each TBP interconversion gives a different ligand permutation. Mechanism M1 corresponds to the Berry pseudorotation. M2 involves a 120° cyclic interchange of one *ax* and two *eq* substituents.<sup>15</sup> It should be noted that the motion in M2 truly resembles that of a mechanical three-arm turnstile gate, whereas the TR mechanism (Scheme 2) performs only half of this motion. In M3, one *ax* and one *eq* substituent interchange by a 180° rotation. M4 leads to complete scrambling of the substituents; the shown “anti-Berry” stereomutation cannot be attained through any of the other mechanisms. In M5, epimerization of the central atom occurs by a 180° interchange of two *eq* groups. Although they are theoretically possible, M4 and M5 have been considered implausible because they proceed through high-energy planar geometries.<sup>14</sup> Thus, herein we

(13) (a) Meakin, P.; Muetterties, E. L.; Jesson, J. P. *J. Am. Chem. Soc.* **1972**, 94, 5271–5285. (b) Russegger, P.; Brickmann, J. *Chem. Phys. Lett.* **1975**, 30, 276–278. (c) Altmann, J. A.; Yates, K.; Csizmadia, I. G. *J. Am. Chem. Soc.* **1976**, 98, 1450–1454. (d) Kutzelnigg, W.; Wasilewski, J. *J. Am. Chem. Soc.* **1982**, 104, 953–960. (e) Wang, P.; Agrafiotis, D. K.; Streitwieser, A.; Schleyer, P. v. R. *Chem. Commun.* **1990**, 201–203. (f) Bento, A. P.; Bickelhaupt, F. M. *Chem.—Asian J.* **2008**, 3, 1783–1792.

(14) (a) Muetterties, E. L. *J. Am. Chem. Soc.* **1969**, 91, 1636–1643. (b) Muetterties, E. L. *J. Am. Chem. Soc.* **1969**, 91, 4115–4122. We use a different numbering of the mechanisms to match their description in terms of multiple Berry deformations. We also note here that Muetterties did not consider the possibility of SP minima.

(15) All five general mechanisms in Scheme 3 involve optimal mappings<sup>10a</sup> and hence are true alternatives. Muetterties<sup>14</sup> also proposed a sixth mechanism in which one *eq* and two *ax* groups permute, but he noted that this mechanism is indistinguishable from M2. This sixth mechanism is transformed into M2 by superimposing a 180° external rotation around one of the nonpermuting *eq* bonds. Both general mechanisms describe the same process using equivalent mappings; which mapping is optimum depends on the chosen reference numbering.<sup>10a</sup>

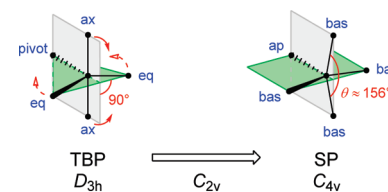
concentrate on M1, M2, and M3 only (animations of these three stereomutation mechanisms for several molecules are available). For these general mechanisms, a limited amount of experimental evidence exists.

Using NMR spectroscopy, Whitesides and co-workers<sup>16</sup> showed that BPR is operative in  $\text{PF}_4\text{NMe}_2$  and  $\text{PF}_4\text{Cl}$  (**3**). A recent two-dimensional IR study<sup>17</sup> showed that the rapid carbonyl scrambling in  $\text{Fe}(\text{CO})_5$  (**4**) is also due to BPR. To date, however, none of the other general stereomutation mechanisms has been verified experimentally. X-ray crystal structures of five-coordinate compounds have also been related to stereomutational mechanisms.<sup>18–22</sup> Geometry distortions in a series of transition-metal complexes were found to follow the Berry coordinate according to a pairing of the face angles.<sup>19</sup> Holmes and co-workers<sup>20</sup> reported similar trends for pentavalent phosphorus and silicon compounds using the dihedral angle sum method. Recently, Alvarez and co-workers<sup>22</sup> arrived at the same conclusion using continuous-shape measures. A drawback of these analyses is that they do not describe the nature of any deviations from the Berry coordinate, which should provide details of the physical stereomutation mechanism. More importantly, the fact that individual structures are distorted along the Berry coordinate does not require that their substituents permute via the BPR mechanism, as we will see.

As an elementary reaction mechanism describes the change in chemical topology from reactant(s) via a transition structure to product(s),<sup>10a,b,12</sup> it can be characterized by the qualitative evolution of geometry along the reaction coordinate. On this basis, we have scrutinized the geometrical changes for stereomutation along the intrinsic reaction coordinate (IRC) pathways for a diverse series of pentavalent compounds whose dynamics have been studied experimentally. By using a set of *internal coordinates*, we will show that this approach enables the determination of the general reaction mechanism by which the substituents interchange. For example, we will formalize how the observed<sup>23</sup> stereomutations of pentaorganylsilicates<sup>24,25</sup> occur via either a BPR or a “double-Berry” mechanism.<sup>25</sup> We will further show that TR as originally defined<sup>10</sup> is equivalent to BPR and distinguish alternative general reaction mechanisms, one of which *does* resemble the motion of a mechanical turnstile gate. Finally, our results are unified using graph theory to afford

- (16) (a) Whitesides, G. M.; Mitchell, H. L. *J. Am. Chem. Soc.* **1969**, *91*, 5384–5386. (b) Eisenhut, M.; Mitchell, H. L.; Traficante, D. D.; Kaufman, R. J.; Deutch, J. M.; Whitesides, G. M. *J. Am. Chem. Soc.* **1974**, *96*, 5385–5397.
- (17) Cahoon, J. F.; Sawyer, K. R.; Schlegel, J. P.; Harris, C. B. *Science* **2008**, *319*, 1820–1823.
- (18) Bürgi, H. B.; Dunitz, J. D. *Acc. Chem. Res.* **1983**, *16*, 153–161.
- (19) Muetterties, E. L.; Guggenberger, L. J. *J. Am. Chem. Soc.* **1974**, *96*, 1748–1756.
- (20) (a) Holmes, R. R.; Deiters, J. A. *J. Am. Chem. Soc.* **1977**, *99*, 3318–3326. (b) Holmes, R. R. *Acc. Chem. Res.* **1979**, *12*, 257–265. (c) Holmes, R. R.; Day, R. O.; Harland, J. J.; Sau, A. C.; Holmes, J. M. *Organometallics* **1984**, *3*, 341–347. (d) Holmes, R. R.; Day, R. O.; Harland, J. J.; Holmes, J. M. *Organometallics* **1984**, *3*, 347–353.
- (21) Bassindale, A. R.; Sohail, M.; Taylor, P. G.; Korlyukov, A. A.; Arkhipov, D. E. *Chem. Commun.* **2010**, *46*, 3274–3276.
- (22) (a) Alvarez, S.; Llunell, M. *J. Chem. Soc., Dalton Trans.* **2000**, 3288–3303. (b) Casanova, D.; Cirera, J.; Llunell, M.; Alemany, P.; Avnir, D.; Alvarez, S. *J. Am. Chem. Soc.* **2004**, *126*, 1755–1763.
- (23) Couzijn, E. P. A.; Schakel, M.; de Kanter, F. J. J.; Ehlers, A. W.; Lutz, M.; Spek, A. L.; Lammertsma, K. *Angew. Chem., Int. Ed.* **2004**, *43*, 3440–3442.
- (24) Couzijn, E. P. A.; Ehlers, A. W.; Schakel, M.; Lammertsma, K. *J. Am. Chem. Soc.* **2006**, *128*, 13634–13639.
- (25) Couzijn, E. P. A.; van den Engel, D. W. F.; Slootweg, J. C.; de Kanter, F. J. J.; Ehlers, A. W.; Schakel, M.; Lammertsma, K. *J. Am. Chem. Soc.* **2009**, *131*, 3741–3751.

**Scheme 4.** Ideal  $C_{2v}$ -Symmetric Berry Coordinate Connecting the TBP and SP Geometries



a general foundation for interpreting the stereomutation of pentavalent molecules.

## Results and Discussion

**Geometry Description.** Pentacoordinate geometries have been described in terms of their displacement along the Berry coordinate from TBP to SP (Scheme 4).<sup>19–21</sup> Ideally, structures along this coordinate retain  $C_{2v}$  symmetry with one *eq* group, the *pivot*, on the  $C_2$  axis. The other four substituents can be divided into two pairs that lie in the two perpendicular symmetry planes: in the *ax,ax*-like pair, the bonds are closer to being collinear, while in the *eq,eq*-like pair, the valence angle is closer to 120°. For perfectly square-pyramidal geometries, the two pairs feature equal valence angles; this so-called trans-basal angle  $\theta$  is typically  $\sim 156^\circ$ .<sup>19,20b,c</sup>

However, most experimental structures deviate from the ideal Berry coordinate. One can discern three distortions: (1) the displaced *ax,ax* and *eq,eq* pairs lie in planes that are not perpendicular; (2) one or both pairs are not coplanar with the pivot bond; and (3) the two atoms of a pair are displaced by unequal amounts. Our geometry analysis includes all of these deviations, as detailed below.<sup>26</sup>

**Atom Assignment.** First, one must determine which bond is the pivot and which ones resemble the *ax* and *eq* bonds. Given the coordinates of six atoms, the atom nearest the centroid is taken to be pentacoordinate, and the two atoms with the largest valence angle are then assigned as (pseudo)axial. The remaining three atoms are (pseudo)equatorial; of these, the pair with the largest valence angle is closest to SP-basal, so the third atom is chosen as the pivot. This assignment is straightforward and avoids arbitrariness in the choice of the pivot atom. The geometrical parameters are defined next.

**Parameterization of Geometry.** Figure 1 illustrates how the seven geometrical parameters used to identify the type of stereomutation along the reaction coordinate are defined. The *ax* and *eq* atoms are fitted by two planes that intersect along the pivot bond and form a dihedral angle  $\delta$ . The *ax* (*eq*) bonds are equally bent out of the *ax* (*eq*) plane by an angle  $\beta_{\text{ax}}$  ( $\beta_{\text{eq}}$ ). The in-plane bond components (represented for the *ax* bonds by the solid projection lines in Figure 1) make an angle  $\theta_{\text{ax}}$  ( $\theta_{\text{eq}}$ ) opposite the pivot atom. The bisector (dashed line in Figure 1) of the angle conjugate to  $\theta_{\text{ax}}$  ( $\theta_{\text{eq}}$ ) (dotted curve in Figure 1) deviates from the pivot by the slanting angle  $\sigma_{\text{ax}}$  ( $\sigma_{\text{eq}}$ ).<sup>27</sup> Finally,  $\theta_{\text{ax}}$  and  $\theta_{\text{eq}}$  are converted to two more meaningful parameters,

- (26) One could argue that because our geometry parameterization is based on the Berry coordinate, our analysis of general stereomutation mechanisms might be biased toward BPR. However, this is not the case, as any reformulation of the internal coordinates leads to the same conclusions, including the one stating that the turnstile rotation is equivalent to BPR. This is shown in section 1.3 of the Addendum in the Supporting Information, in which an alternative analysis based on the TR coordinate is used.
- (27) The signs of  $\beta_{\text{ax}}$  and  $\beta_{\text{eq}}$  and of  $\sigma_{\text{ax}}$  and  $\sigma_{\text{eq}}$  depend on the input ordering of the atoms, as does the direction in which  $\delta$  deviates from 90°.

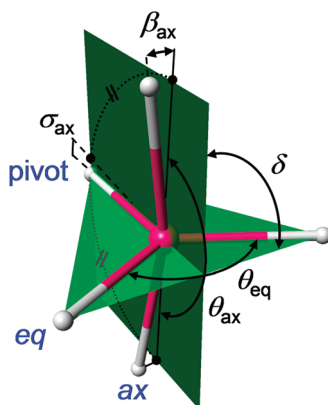


**Figure 1.** Geometry analysis. The definitions of  $\beta_{\text{eq}}$  and  $\sigma_{\text{eq}}$  have been omitted for clarity.

the topology parameter (TP) and the average trans angle ( $\bar{\theta}$ ), as follows:

$$\text{TP} = \frac{\theta_{\text{ax}} - \theta_{\text{eq}}}{60^\circ} \quad \text{and} \quad \bar{\theta} = \frac{3}{5}\theta_{\text{ax}} + \frac{2}{5}\theta_{\text{eq}}$$

The TP, which expresses the distortion along the Berry coordinate, ranges from 1 for an ideal TBP to 0 for an ideal SP geometry;<sup>28</sup>  $\bar{\theta}$  indicates the development of the trans-basal angle along the Berry coordinate and includes a 3:2 weighting to account for the experimentally observed higher flexibility of the eq bonds relative to the ax bonds.<sup>19,20b,c</sup> These seven independent parameters (TP and the angles  $\bar{\theta}$ ,  $\delta$ ,  $\sigma_{\text{ax}}$ ,  $\sigma_{\text{eq}}$ ,  $\beta_{\text{ax}}$ , and  $\beta_{\text{eq}}$ ) fully describe the bond directions in any pentavalent geometry.<sup>1,27</sup> When the progression of a molecular structure along a stereomutation pathway is being analyzed, the parameter that changes most prominently and consistently is the one that best describes the general mechanism that is operative. The actual lengths of the five bonds are not relevant for the stereomutational analysis, which concerns only intramolecular (i.e., nondissociative) substituent interchange.

**Analysis of Substituent Permutations.** Muetterties' stereomutations were examined for the representative set of pentavalent main-group and transition-metal compounds shown in Chart 1, which includes acyclic, spirocyclic, and caged structures. The chart lists the relative Gibbs free energies of the stereoisomers of each system, which were calculated using the following density functional theory (DFT) methods:<sup>29</sup> B3LYP/6-311++G(2d,p) for **1** and **3**; B3LYP/6-311++G(2d,p)//B3LYP/6-31G(d) for **2** and **7–11**; and B3PW91/SDB-cc-pVTZ<sup>30</sup>//B3PW91/SDD(d) for **4–6** (see the Computational Section). Each system has been the subject of experimental study, and all but the bracketed stereoisomers have been observed. Table 2 lists the calculated stereomutation barriers together with reported experimental values; the agreement between them is good to excellent. For the epimerization of **7**, we previously validated the DFT method against the wave-function-based SCS-MP2/6-311++G(2d,p)//MP2/6-31G(d) method.<sup>25</sup> Moreover, the

- (28) The TP parameter differs from the  $\tau$  parameter introduced in the following reference: Addison, A. W.; Rao, T. N.; Reedijk, J.; van Rijn, J.; Verschoor, G. C. *J. Chem. Soc., Dalton Trans.* **1984**, 1349–1356 (also see ref 22a). We use projected trans valence angles in order to separate out any contribution from out-of-plane distortions  $\beta$ .
- (29) Frisch, M. J.; et al. *Gaussian 03*, revision C.02; Gaussian, Inc.: Wallingford, CT, 2004.
- (30) Martin, J. M. L.; Sundermann, A. *J. Chem. Phys.* **2001**, *114*, 3408–3420.

**Table 2.** Calculated and Reported Experimental Gibbs Free Energy Barriers  $\Delta^{\ddagger}G$  (in kcal mol<sup>-1</sup>) for Stereomutations of **1–11**<sup>a</sup>

stereomutation	Muetterties' mechanism <sup>b</sup>	observed			
		$\Delta^{\ddagger}G_{\text{calcd}}$	$\Delta^{\ddagger}G_{\text{exptl}}$	<i>T</i> (K)	ref.
<b>1</b> $\rightleftharpoons$ <b>1'</b>	M1	3.8 <sup>c</sup>	3.1(2) <sup>c</sup>	298	4
<b>2</b> $\rightleftharpoons$ <b>2'</b>	M1	0.8	<5	108	10b, d, e
<b>3.I</b> $\rightleftharpoons$ <b>3.I'</b>	M1	4.1	4.2(3)	96	16b
<b>3.I</b> $\rightleftharpoons$ <b>[3.II]</b>	M1	4.8			
<b>4</b> $\rightleftharpoons$ <b>4'</b>	M1	2.0 <sup>d</sup>	1.6(3) <sup>d</sup>	323	17
<b>5.I</b> $\rightleftharpoons$ <b>5.I'</b>	M2	13.3			
<b>5.I</b> $\rightleftharpoons$ <b>5.II</b>	M2	10.5	11	243	34a
<b>6.I</b> $\rightleftharpoons$ <b>6.I'</b>	M2	13.8			
<b>6.I</b> $\rightleftharpoons$ <b>6.II</b>	M2	12.3	13 <sup>e</sup>	273	34b
<b>6.II</b> $\rightleftharpoons$ <b>6.II'</b>	M2	8.2			
<b>Δ-7</b> $\rightleftharpoons$ <b>Δ-7</b>	M2	11.1	13	247	25, 35
	M1	16.3			
<b>Δ-8.I</b> $\rightleftharpoons$ <b>[Δ-8.III]</b>	M1	11.3	15.5(5) <sup>f</sup>	258	23, 25
<b>Δ-8.II</b> $\rightleftharpoons$ <b>[Δ-8.III]</b>	M2	13.9			
<b>Δ-8.II</b> $\rightleftharpoons$ <b>Δ-8.II</b>	M1	12.9			
<b>Δ-8.I</b> $\rightleftharpoons$ <b>Δ-8.II</b>	M2	17.1			
<b>9.I</b> $\rightleftharpoons$ <b>9.II</b>	M3	27.3	28.5(9)	363	33
<b>10.I</b> $\rightleftharpoons$ <b>10.II</b>	M3	15.9	19 <sup>e</sup>	347	36
<b>11.I</b> $\rightleftharpoons$ <b>[11.II]</b> $\rightleftharpoons$ <b>11.I'</b>	"M3" <sup>g</sup>	10.2	12	247	36

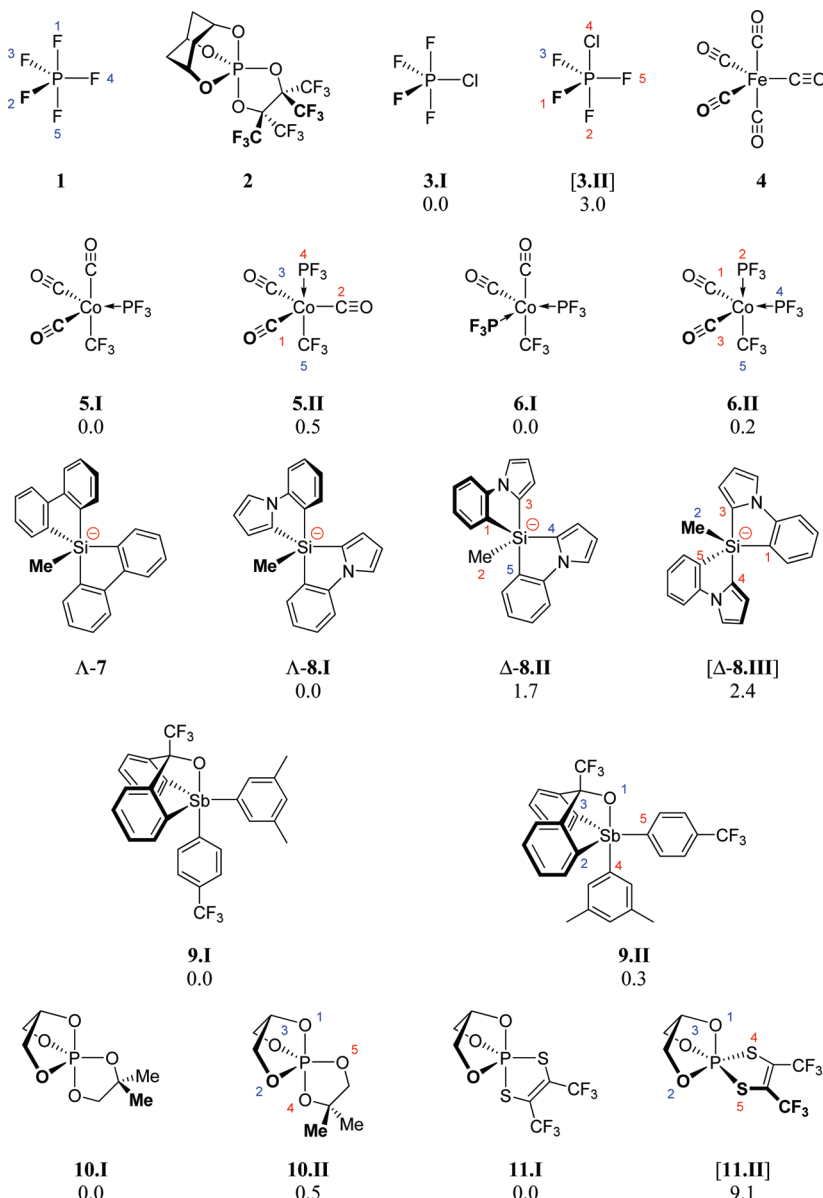
<sup>a</sup> The reported values of  $\Delta^{\ddagger}G$  are relative to the most stable stereoisomer; see the text for the DFT methods used for  $\Delta^{\ddagger}G_{\text{calcd}}$ . Stereoisomers shown in brackets have not been observed experimentally.

<sup>b</sup> Muetterties' mechanisms are described in Scheme 3 and the accompanying text. Animations of the stereomutational mechanisms M1–M3 for **2**, **3**, **5**, and **10** (including equilibrium geometries and transition structures) are available. <sup>c</sup> Energy barrier  $\Delta^{\ddagger}E$ . <sup>d</sup> Activation energy  $E_a$ . <sup>e</sup> Estimated from the reported NMR coalescence phenomena according to ref 37. <sup>f</sup> Overall barrier for **Δ-8.I**  $\rightleftharpoons$  **[Δ-8.III]**  $\rightleftharpoons$  **Δ-8.II** (see ref 25). <sup>g</sup> See the text.

optimized geometries and X-ray structures of **1**,<sup>2</sup> **4**,<sup>31</sup> **7**,<sup>32</sup> **8.I**,<sup>23</sup> and **9.I**<sup>33</sup> show very similar bond directions around the pentavalent centers (see the Supporting Information); the minor differences in bond lengths are of no relevance to the analyses. Because of the close resemblance of the computed geometries to those observed experimentally, the calculated geometrical changes are also expected to accurately describe the physical stereomutation mechanisms.

To characterize the substituent interchange mechanisms for **1–11** (Chart 1), we parametrized the geometries along the corresponding minimum-energy IRC pathways using an algorithm that was coded in Turbo Delphi<sup>38</sup> to automate the analysis of multistructure XYZ files. Plots of each of the parameters (TP,  $\bar{\theta}$ ,  $\delta$ ,  $\sigma_{\text{eq}}$ ,  $\beta_{\text{ax}}$ , and  $\beta_{\text{eq}}$ ) against the reaction coordinate for each stereomutation are included in the Supporting Information. The topology parameter TP turned out to change most prominently and in a consistent and distinct manner for each general mechanism. The angle parameters varied little for the acyclic systems (**1** and **3–6**), whereas larger changes in the

- (31) Braga, D.; Grepioni, F.; Orpen, A. G. *Organometallics* **1993**, *12*, 1481–1483.
- (32) (a) Deerenberg, S.; Schakel, M.; de Keijzer, A. H. J. F.; Kranenburg, M.; Lutz, M.; Spek, A. L.; Lammertsma, K. *Chem. Commun.* **2002**, 348–349. (b) Ballweg, D.; Liu, Y. X.; Guzei, I. A.; West, R. *Silicon Chem.* **2002**, *1*, 57–60.
- (33) Matsukawa, S.; Yamamichi, H.; Yamamoto, Y.; Ando, K. *J. Am. Chem. Soc.* **2009**, *131*, 3418–3419.
- (34) (a) Udovich, C. A.; Clark, R. J. *J. Am. Chem. Soc.* **1969**, *91*, 526–527. (b) Udovich, C. A.; Krevalis, M. A.; Clark, R. J. *Inorg. Chem.* **1976**, *15*, 900–905.
- (35) de Keijzer, A. H. J. F.; de Kanter, F. J. J.; Schakel, M.; Osinga, V. P.; Klumpp, G. W. *J. Organomet. Chem.* **1997**, *548*, 29–32.
- (36) Campbell, B. S.; De'Ath, N. J.; Denney, D. B.; Denney, D. Z.; Kipnis, I. S.; Min, T. B. *J. Am. Chem. Soc.* **1976**, *98*, 2924–2927.

Chart 1. Investigated Systems 1–11<sup>a</sup>

<sup>a</sup> The general substituent numbering is given for **1**. Red numbers are used for the permuted substituents of the minor isomers for which the calculated relative  $\Delta G$  values (in kcal mol<sup>-1</sup> at the temperatures given in Table 2) are also listed.

slanting angles  $\sigma_{ax}$  and  $\sigma_{eq}$  were found for the geometrically constrained systems with bi- and tridentate substituents (**2** and **7–11**). The angle parameters did not show a coherent relationship with any of the stereomutational mechanisms, and we infer that they reflect secondary geometry deformations (see below). Throughout this paper, we focus mainly on the topology parameter TP for our analysis of the general perturbation mechanisms, and only where necessary for a better understanding are other parameters discussed. We first inspect the established Muettterties' mechanism M1 (i.e., BPR) and compare it with TR before turning to mechanisms M2 and M3.

**M1: Berry Pseudorotation.** The degenerate fluorine interchange in  $\text{PF}_5$  (**1**) is exemplary of a BPR (Scheme 1). The energy profile for the reaction coordinate of this process is shown in the left panel of Figure 2 (black) together with the behavior of the TP (red). As expected, the TP nicely reflects the concept of the Berry pseudorotation, decreasing linearly from 1 for the minimum-energy TBP structure to 0 for the SP

transition structure and back to 1 for the permuted TBP structure. The average trans angle  $\bar{\theta}$  (Figure 2, right) changes only slightly, and its curvature reflects the fact that the bending of the *ax* bonds slightly lags that of the *eq* bonds. The other geometrical parameters do not deviate from their ideal values ( $90^\circ$  for  $\delta$ ;  $0^\circ$  for  $\sigma_{ax}$ ,  $\sigma_{eq}$ ,  $\beta_{ax}$ , and  $\beta_{eq}$ ) for symmetry reasons.

The symmetry of the substituent interchange is reduced when a fluorine atom in  $\text{PF}_5$  is replaced by chlorine to give  $\text{PF}_4\text{Cl}$  (**3**). As a result, two BPR stereomutations for the global minimum-energy structure **3.I** become feasible, namely, a degenerate exchange of the *ax* and *eq* fluorine pairs (**3.I'**; Figure 3, left) and a nondegenerate one in which the two *ax* fluorines are exchanged for one *eq* fluorine and the *eq* chlorine atom ([**3.II**]; Figure 3, right). The *eq* chlorine serves as pivot in the degenerate BPR, as opposed to an *eq* fluorine in the nondegenerate BPR. The energy profiles and related behaviors of the TP for both processes are shown in the lower part of Figure 3. For the degenerate BPR, the trend in the TP parallels that for  $\text{PF}_5$ ,

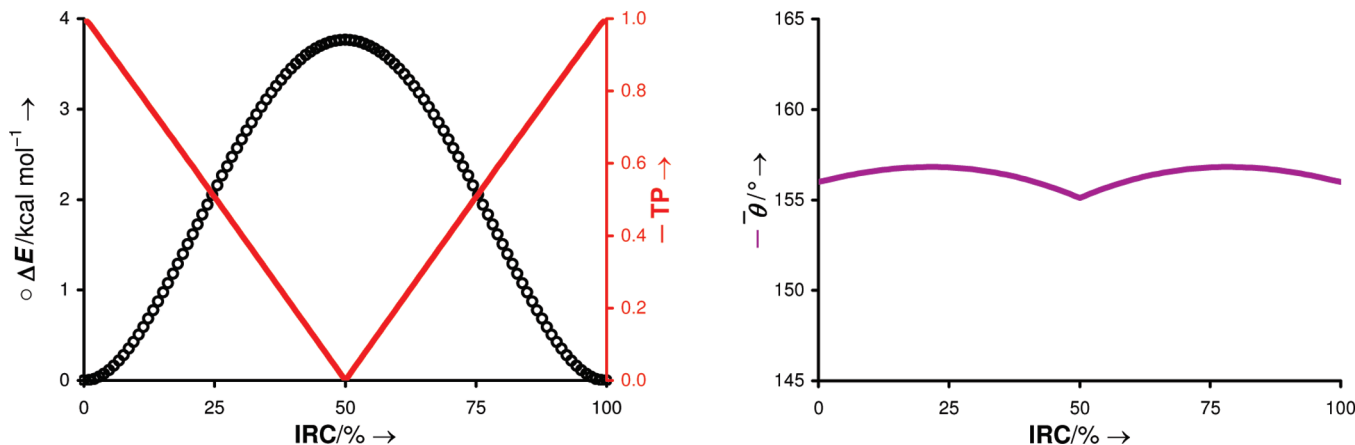


**Figure 2.** BPR pathway for  $\text{PF}_5$  (**1**): (left) relative energy  $\Delta E$  (black) and topology parameter TP (red) and (right) average trans angle  $\bar{\theta}$  along the intrinsic reaction coordinate (IRC).

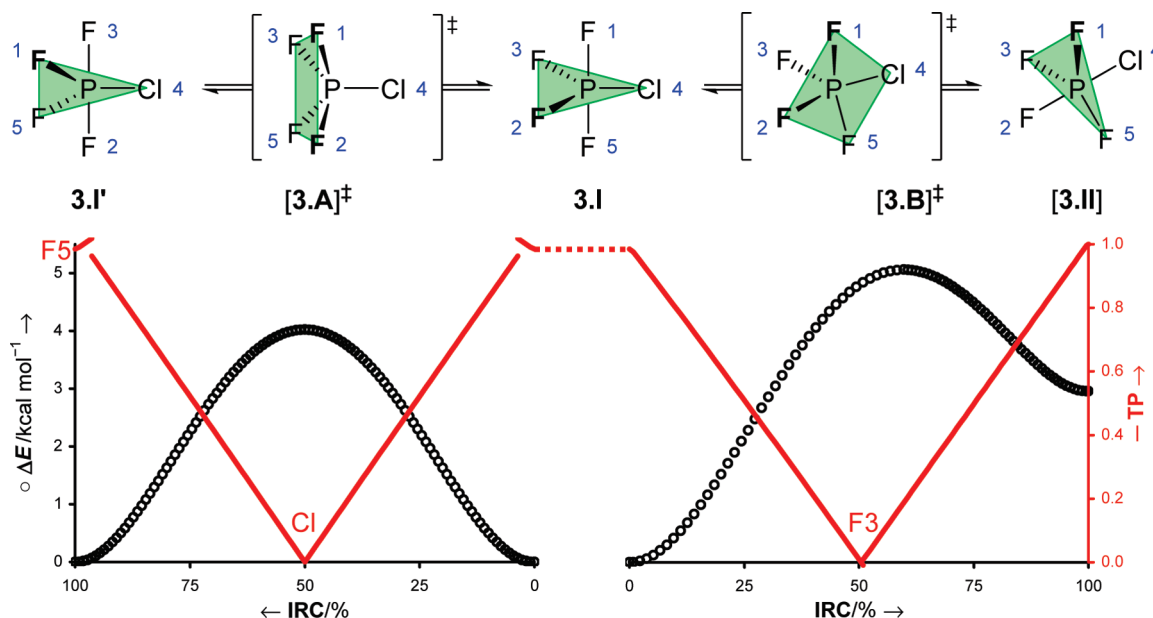
as it decreases linearly to 0 when it reaches the SP transition structure  $[\mathbf{3.A}]^{\ddagger}$  and then increases again to  $\sim 1$  for the permuted structure  $\mathbf{3.I}'$ . The discontinuities near the minima are due to a slight displacement of the fluorines away from the larger chlorine substituent, and as a consequence, the algorithm assigns an *eq* fluorine as the pivot for these slightly distorted TBPs.

The nondegenerate process in which **3.I** is converted to the 3.0 kcal mol<sup>-1</sup> less stable **3.II** shows the same V-shaped trend in the TP as for  $\mathbf{3.I} \rightleftharpoons \mathbf{3.I}'$ . Interestingly, whereas the TP minimum is again located halfway along the reaction coordinate, the fully developed transition structure  $[\mathbf{3.B}]^{\ddagger}$  is reached later and consequently already has 19% TBP character. This behavior reflects the Hammond postulate,<sup>39</sup> illustrating that the geometry of the TS bears some resemblance to that of the less stable isomer **3.II**. Nevertheless, the TP signature for the  $\mathbf{3.I} \rightleftharpoons \mathbf{3.II}$  stereomutation shows the same topological changes as that for the degenerate process, identifying them both as Berry pseudorotations.

The transition-metal complex  $\text{Fe}(\text{CO})_5$  (**4**) shows the same TP behavior as discussed for  $\text{PF}_5$  and is therefore not discussed here. The graphs for **4** are presented in the Supporting Information.

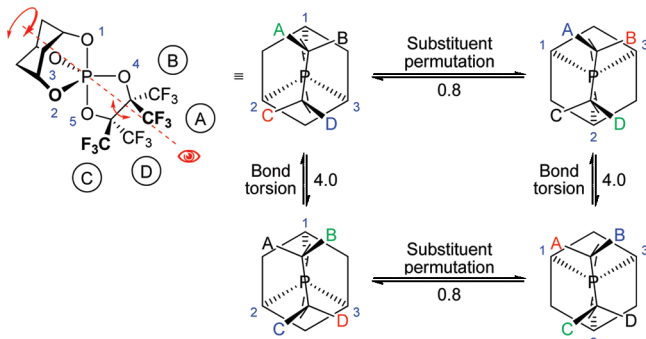
**Turnstile Rotation versus Berry Pseudorotation.** So far, we have discussed the behavior of the TP for the Berry pseudorotation and shown that it gives a single-V-shaped profile along the reaction coordinate. But what is the TP behavior for the other well-known permutation, the turnstile rotation? We focus on the caged oxyphosphorane **2**, whose extreme nonrigidity led to the proposal of the TR mechanism.<sup>10</sup> On the basis of the progressive broadening of the  $^{19}\text{F}$  NMR resonances at low temperatures, a permutation barrier of  $\Delta^{\ddagger}G_{108\text{K}} < 5$  kcal mol<sup>-1</sup> was reported.<sup>10d,e</sup> However, our calculated barrier for this process, indicated by the horizontal arrows in Scheme 5, is only 0.8 kcal mol<sup>-1</sup> at 108 K. Such a low barrier cannot be responsible for the observed NMR line broadening. Instead, we ascribe this effect to the torsion of the central C–C bond in the bidentate substituent (shown by the vertical arrows in Scheme 5), which has a calculated barrier of  $\Delta^{\ddagger}G_{108\text{K}} = 4.0$  kcal mol<sup>-1</sup>. This still leaves the question of what the signature of the permutation is.

Figure 4 depicts the energy profile as well as the behavior of the TP (left) and the slanting angles  $\sigma_{\text{ax}}$  and  $\sigma_{\text{eq}}$  (right) along the permutational reaction coordinate of **2**. The trend in TP is a single-V-shaped form, thereby suggesting that the topology



**Figure 3.** (top) The two BPR pathways for  $\text{PF}_4\text{Cl}$ : (left)  $\mathbf{3.I} \rightleftharpoons \mathbf{3.I}'$ ; (right)  $\mathbf{3.I} \rightleftharpoons \mathbf{3.II}$ . (bottom) corresponding plots of the relative energy  $\Delta E$  (black) and topology parameter TP (red) along the IRC; the pivot atom is specified in each plot.

**Scheme 5.** Schematic Projection of **2** along the Depicted Red Axis with Calculated  $\Delta^{\ddagger}G_{108K}$  Barriers (in kcal mol<sup>-1</sup>)<sup>a</sup>



<sup>a</sup> The colors indicate how the chemical environments of the CF<sub>3</sub> moieties A–D interchange by permutation (horizontal arrows) and diolate C–C bond torsion (vertical arrows).

changes according to a BPR process with an *eq* adamantoid oxygen as the pivot atom. The 4% offset of the minimum and the transition structure along the IRC from the most TBP- and SP-like geometries, respectively, originates from the asymmetry introduced by the staggered central C–C bond of the bidentate substituent. The large slanting angles at either end of the reaction coordinate reflect the constraints imposed on the minimum-energy geometry of **2** by the cage motif, which forces the adamantoid *eq, eq* valence angle to decrease from the ideal value of 120° to 107.2° and the *ax, eq* valence angles to increase from their ideal value of 90° to 97.1°.<sup>40</sup> As the geometry of **2** progresses toward the transition structure, both slanting angles approach 0° because the adamantoid valence angles approach those of an ideal SP geometry. Thus, the analysis suggests that **2** permutes via BPR and that the low barrier is attributable to relief of cage strain in the TS.

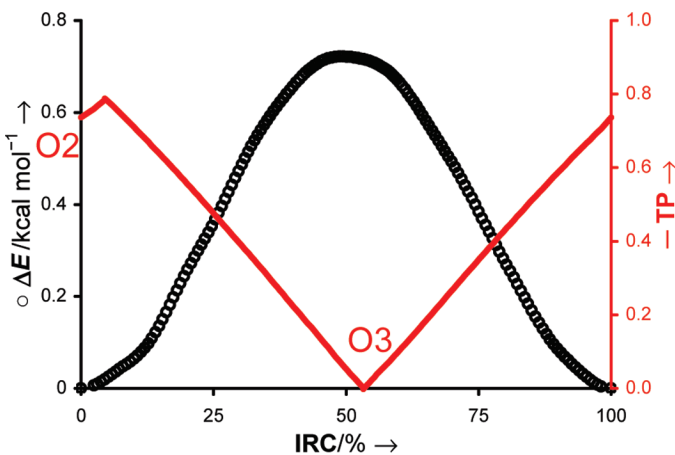
Can this BPR assignment of the permutation of **2** be confirmed? The atomic displacements for the imaginary vibrational mode of the transition structure may provide such insight.<sup>33</sup> Although the transition vector for [2.A]<sup>‡</sup> (Figure 5, left) seems to resemble a TR motion with rotation of the tridentate and bidentate groups in opposite directions rather than a BPR motion (see Scheme 2 vs M1 in Scheme 3), this is misleading.<sup>13e,f</sup> Not only is the amplitude for rotation of the bidentate group very small, but also, the adamantoid oxygen atoms do not contribute equally to the opposite rotation of the tridentate group, with the amplitude on the *ap* oxygen being

about half of the other two amplitudes. A BPR-like transition vector would result by simply subtracting the rotational motion of the *ap* oxygen atom from all of the contributions, that is, by superimposing a rotation of the whole molecule in the same direction in which the bidentate substituent is turning.

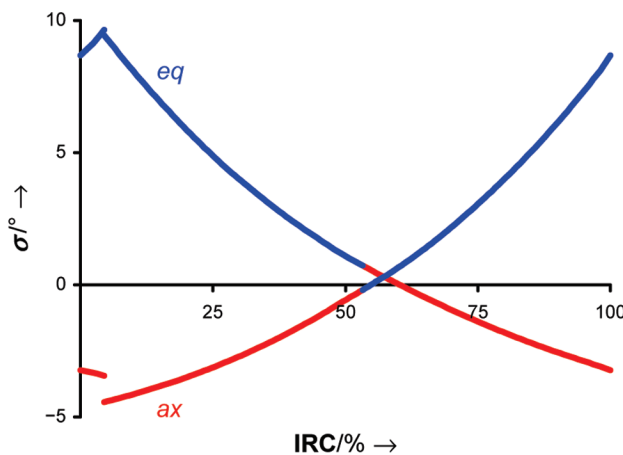
This paradox stems from the fact that the vibrational mode describes the *mass-weighted* relative atomic movements.<sup>41</sup> Thus, the molecular deformation in **2** is mainly expressed as a rotation of the light tridentate substituent (129 amu), whereas the much heavier bidentate substituent (332 amu) remains almost in place. When the bidentate group in **2** is replaced by a cyclobutane-1,3-diolate substituent as in [12.A]<sup>‡</sup> (Figure 5, right), all alkoxy moieties become identical [i.e., (OCH<sub>2</sub>)<sub>n</sub> (*n* = 2, 3)], which should cause the mass-weighted movements of the four basal groups to cancel. Indeed, the transition vector of [12.A]<sup>‡</sup> has no amplitude on the *ap* oxygen atom<sup>42</sup> and resembles a regular BPR motion. This example thus shows that the presence of the adamantanoid moiety does *not* prohibit a BPR or necessitate a TR mechanism.<sup>10</sup>

The same phenomenon can be illustrated for PH<sub>3</sub>T<sub>2</sub> and PH<sub>5</sub>, both of which perform true BPR motions (Figure 6). However, in contrast to PH<sub>5</sub>, the imaginary vibrational mode of PH<sub>3</sub>T<sub>2</sub> suggests a TR-type internal rotation of the hydrogen trio versus the pair of tritium atoms. Because of the larger mass of the tritium atoms, the BPR motion in PH<sub>3</sub>T<sub>2</sub> is superimposed by an overall rotation that can be readily visualized by subtracting the imaginary vibrational mode of PH<sub>5</sub> from that of PH<sub>3</sub>T<sub>2</sub> (Figure 6, middle).

The foregoing discussion raises the question of whether the general BPR and TR mechanisms are truly different.<sup>13</sup> TR was claimed to be an alternative principal stereomutational mechanism to BPR because of their different permutational schemes, which follow from optimal mapping of the stereomutated structures onto the original one.<sup>10a,15</sup> As a TBP has three *eq* but only two *ax* sites, at least one substituent remains *eq* regardless of the stereomutation, and hence, no principal mechanism can permute all sites. However, the permutational scheme presented for TR<sup>10</sup> does affect all sites. Spatial reorientation of the stereomutated molecule relative to the reactant affords a simpler permutational scheme, namely, that of BPR (see section 1.2 of the Addendum in the Supporting Information).<sup>13e,f</sup> We therefore conclude that the ideal TR and BPR mechanisms merely describe alternative model motions for the same general reaction mechanism and that the external rotation superimposed for TR makes it *seem* different from BPR.



**Figure 4.** Permutation of **2**: (left) relative energy  $\Delta E$  (black) and topology parameter TP (red) along the IRC; (right) slanting angles  $\sigma_{\text{ax}}$  (red) and  $\sigma_{\text{eq}}$  (blue) along the IRC.



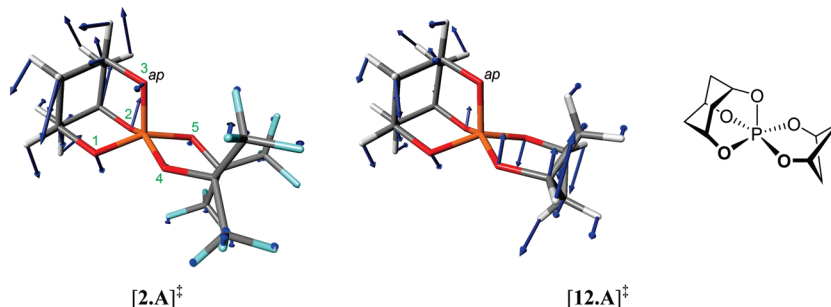


**Figure 5.** Imaginary vibrational modes of the permutational transition structures of (left) caged oxyphosphorane **2** and (right) cyclobutane-1,3-diolate analogue **12**.

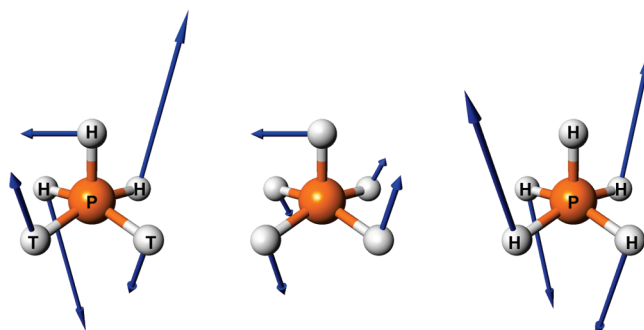


**Figure 6.** Imaginary vibrational modes of the permutational transition structures of PH<sub>3</sub>T<sub>2</sub> (left), PH<sub>5</sub> (right), and their difference (middle).

An important advantage of our analysis is that complications due to such external reorientations are inherently avoided by the use of internal coordinates. Next, we examine whether there is support for the other mechanisms suggested by Muetterties (Scheme 3).<sup>14</sup>

**M2: Threefold Cyclic Permutation.** As first example to illustrate general mechanism M2, we address the stereodynamics of the two minima of the cobalt complex Co(CO)<sub>3</sub>(CF<sub>3</sub>)(PF<sub>3</sub>) (**5**; Chart 1), which has been studied experimentally by Udovich and Clark.<sup>34</sup> Both conformers have an approximate TBP geometry; the *ax* CF<sub>3</sub> group is opposite a CO in **5.I** and the PF<sub>3</sub> group in the only 0.5 kcal mol<sup>-1</sup> less stable **5.II**. The top portion of Figure 7 shows the two possible stereomutations, a degenerate cyclic permutation of the three CO groups (**5.I** ⇌ **5.I'**, left) with a barrier of 13.3 kcal mol<sup>-1</sup> and a nondegenerate cyclic interchange of the PF<sub>3</sub> and two CO groups (**5.I** ⇌ **5.II**, right) with a slightly lower barrier of 10.5 kcal mol<sup>-1</sup>. The corresponding transition structures [**5.A**]<sup>‡</sup> and [**5.B**]<sup>‡</sup> for these processes also resemble TBP geometries, as do the minimum-energy structures to which they are related by a single Berry-

type motion. In BPR, both *ax* substituents exchange with *eq* ones, but moving the highly electronegative CF<sub>3</sub> group in **5** to an *eq* TBP position is undesirable and results in a TS rather than a minimum; a subsequent Berry-type deformation returns the *eq* CF<sub>3</sub> group back to an *ax* position.

The occurrence of a double Berry deformation in both processes is nicely reflected by the behavior of the TP along the IRCs, which features a double-V shape as shown in the two graphs in Figure 7. The degenerate process that converts **5.I** into **5.I'** has the *eq* C(2)O group as the pivot for the first Berry motion, which provides transition structure [**5.A**]<sup>‡</sup>, and then the C(1)O group, which has moved to an *eq* position, becomes the pivot for the subsequent deformation to **5.I'**. Only at the onset and the very end of the stereomutation does the PF<sub>3</sub> group function as the pivot because of the slightly distorted TBP geometry of **5.I** (**5.I'**), an aspect we discussed above for PF<sub>4</sub>Cl (**3**). The nondegenerate stereomutation of **5.I** to **5.II** starts with a simple Co—P bond rotation for ~18% of the IRC, at which point the first Berry motion occurs with the PF<sub>3</sub> group acting as the pivot to provide the TS [**5.B**]<sup>‡</sup>, which undergoes the second deformation to **5.II** using the C(1)O group as the pivot. As expected for these stereomutations, the structures at the cusps of the double-V-shaped TP graphs in Figure 7 are nonstationary SP-like geometries, namely, [**5.I-A**] and [**5.I-A'**] for the degenerate permutation and [**5.I-B**] and [**5.II-B**] for the non-degenerate stereomutation (Figure 8). This analysis shows that Muetterties' general mechanism M2 entails two consecutive Berry-type motions in a single step; it differs from a double BPR by having a single energy barrier.

We next turn to the cobalt complex Co(CO)<sub>2</sub>(CF<sub>3</sub>)(PF<sub>3</sub>)<sub>2</sub> (**6**). Its reported <sup>19</sup>F NMR spectra show a triplet for the CF<sub>3</sub> group that below 0 °C splits into two triplets having unequal intensities, with the smaller one evolving into a doublet at -90 °C.<sup>34b</sup> In agreement with these observations, we found that the minimum **6.I** and the only 0.2 kcal mol<sup>-1</sup> less stable **6.II** undergo three stereomutations (Scheme 6), namely, a degenerate one for each conformer and a nondegenerate one that interconverts the two. The corresponding barriers are Δ<sup>‡</sup>G<sub>273K</sub> = 13.8, 8.2, and 12.3 kcal mol<sup>-1</sup> for the permutations of **6.I** and **6.II** and the **6.I** → **6.II** interconversion, respectively. The degenerate ligand permutation in **6.II** is sufficiently fast at temperatures above -90 °C for the *ax* and *eq* phosphorus atoms to become equivalent on the NMR time scale, causing the phosphorus-coupled CF<sub>3</sub> <sup>19</sup>F NMR resonance to collapse from a double doublet into a triplet.<sup>34b</sup>

Our analyses show that each of the three perturbations follows Muetterties' mechanism M2 involving a double Berry deformation, as reflected by the double-V-shaped profile of the TP (see the Supporting Information). The behavior of this system is

- (37) Friebolin, H. *Basic One- and Two-Dimensional NMR Spectroscopy*, 3rd ed.; Wiley-VCH: Weinheim, Germany, 1998; Chapter 11.
- (38) *Turbo Delphi for Microsoft Windows*, version 10, update 2; Borland Software Corporation: Austin, TX, 2005.
- (39) Hammond, G. S. *J. Am. Chem. Soc.* **1955**, 77, 334–338.
- (40) The discontinuities in the slanting angles σ<sub>ax</sub> and σ<sub>eq</sub> (Figure 4, right) at 4% of the reaction coordinate are due to the reassignment of the pivot atom (from *eq* O2 to *eq* O3), while those at 54% are the result of the reassignment of the *ax,ax* and *eq,eq* pairs upon passing through the most SP-like structure.
- (41) Wilson, E. B., Jr.; Decius, J. C.; Cross, P. C. *Molecular Vibrations: The Theory of Infrared and Raman Vibrational Spectra*; Dover Publications: New York, 1980.
- (42) Actually, a high-precision printout of the transition vector revealed a very small O<sup>ap</sup> contribution that even *opposes* the rotation of the adamantoid O<sup>bas</sup> atoms. The angular momenta of all of the other atoms do not exactly cancel because the two substituents have slightly different bond lengths and angles.

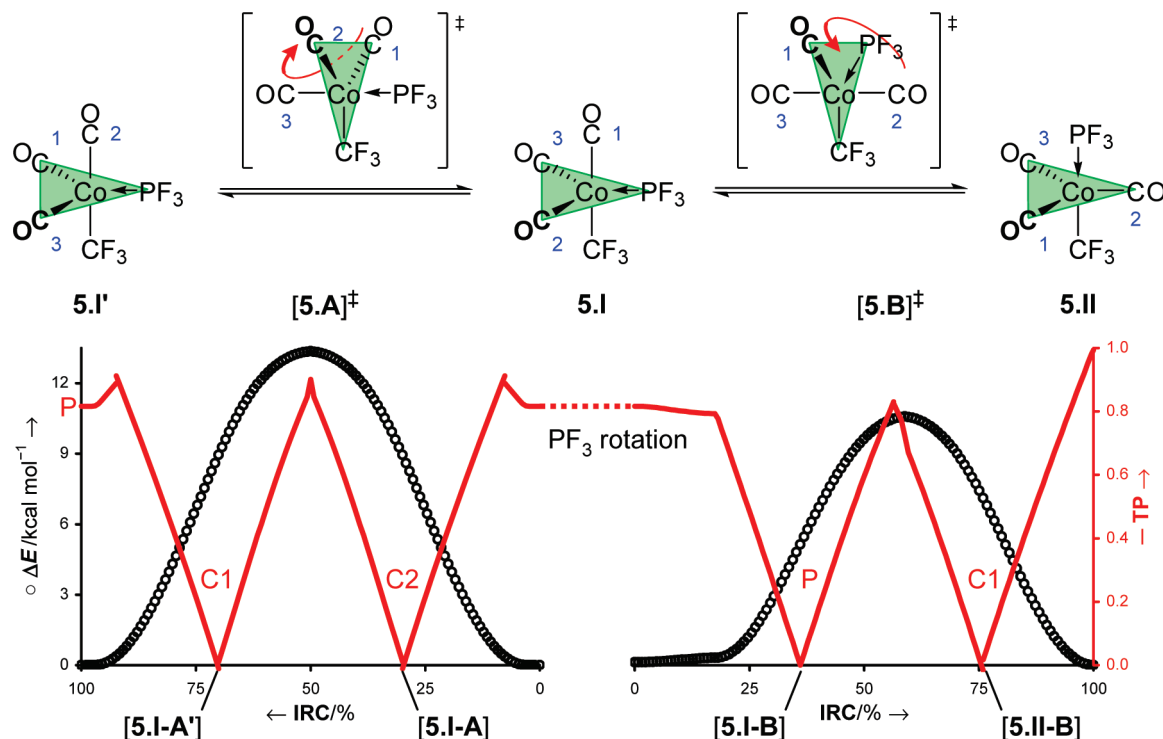


**Figure 7.** (top) Stereomutations of **5** and (bottom) corresponding plots of relative energy  $\Delta E$  (black) and the TP (red) along the IRCs. The pivot atoms are indicated in each plot.

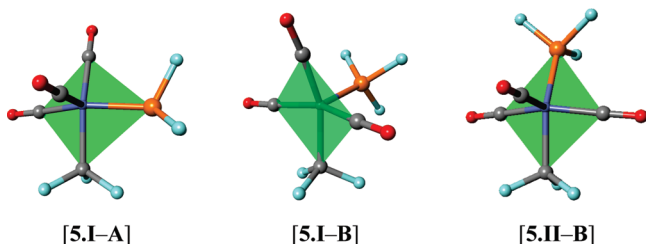
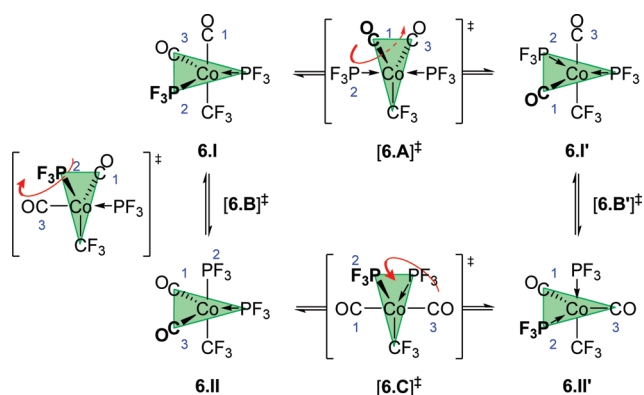


**Figure 8.** Nonstationary SP-like geometries at the cusps of the double-V-shaped TP graphs for the stereomutations **5.I** ⇌ **5.I'** (left) and **5.I** ⇌ **5.II** (middle, right) shown in Figure 7.

**Scheme 6. Stereomutations of 6**



reminiscent of that discussed for **5** with the extension that in addition to **6.I**, **6.II** can also undergo a degenerate permutation.

**M1 and M2 in the Same System.** So far, we have discussed molecules that undergo substituent interchange via either Muettterties' mechanism M1 or M2, but there are also systems

such as the spirocyclic pentaorganylsilicates **7** and **8**<sup>25</sup> in which both mechanisms are operative. We first discuss the fluxionality of **7**.

Each biphenyl-2,2'-diyl moiety in **7** prefers an *ax,eq*-bridging arrangement, affording a propeller-like structure that can be left- or right-handed ( $\Lambda$  or  $\Delta$ ). As shown in Figure 9, inversion of helicity can occur either by a BPR with the methyl substituent as the pivot (left) or by a double Berry deformation (right) in which first the *eq* aryl moiety and then the other aryl moiety of one of the biphenyl-2,2'-diyl groups acts as the pivot (i.e., atoms C3 and C1, respectively).<sup>25</sup> The SP-like TS **[7.A]‡** for epimerization via general mechanism M1 (single-V-shaped TP) suffers from steric hindrance between the ortho hydrogen atoms of the two *bas,bas* biphenyl groups ( $\Delta^{\ddagger}G_{273K} = 16.3 \text{ kcal mol}^{-1}$ ), whereas instead the TBP-like TS **[7.B]‡** of general mechanism M2 (double-V-shaped TP) carrying a biphenyl substituent bridging two *eq* sites (C1 and C3; Figure 9) is destabilized ( $\Delta^{\ddagger}G_{273K} = 11.1 \text{ kcal mol}^{-1}$ ) by the repulsive interactions between the *eq,eq* biphenyl  $\pi$  system and the electron-rich axial bonds.<sup>24</sup> **[7.B]‡** shows an unusually large slanting angle  $\sigma$  due to the constrained *eq,eq* endocyclic C–Si–C angle that pulls the pivot group away from an ideal TBP orientation (Figure 9, bottom right), while in mechanism M1, this constraint brings the *ax* and *eq* planes out of orthogonality ( $\delta$ ; Figure 9, bottom left).

Desymmetrization of the biaryl ligands in **7**, such as by the use of the two phenylpyrrol-2,2'-diyl moieties in pentaorganylsilicate **8**, produces three enantiomeric pairs of configurational isomers (**8.I–III** in the case of **8**).<sup>23,25</sup> Scheme 7 shows the possible interchange pathways. The displayed vertical isomerizations  $\Lambda\text{-}8.\text{I} \rightleftharpoons [\Delta\text{-}8.\text{III}]$  and  $\Delta\text{-}8.\text{II} \rightleftharpoons \Lambda\text{-}8.\text{II}$  follow the general BPR mechanism (single-V-shaped TP profile) and have SP-like transition structures **[8.A]‡** and **[8.C]‡**, respectively, with the methyl group at the apical site. The horizontal isomerizations

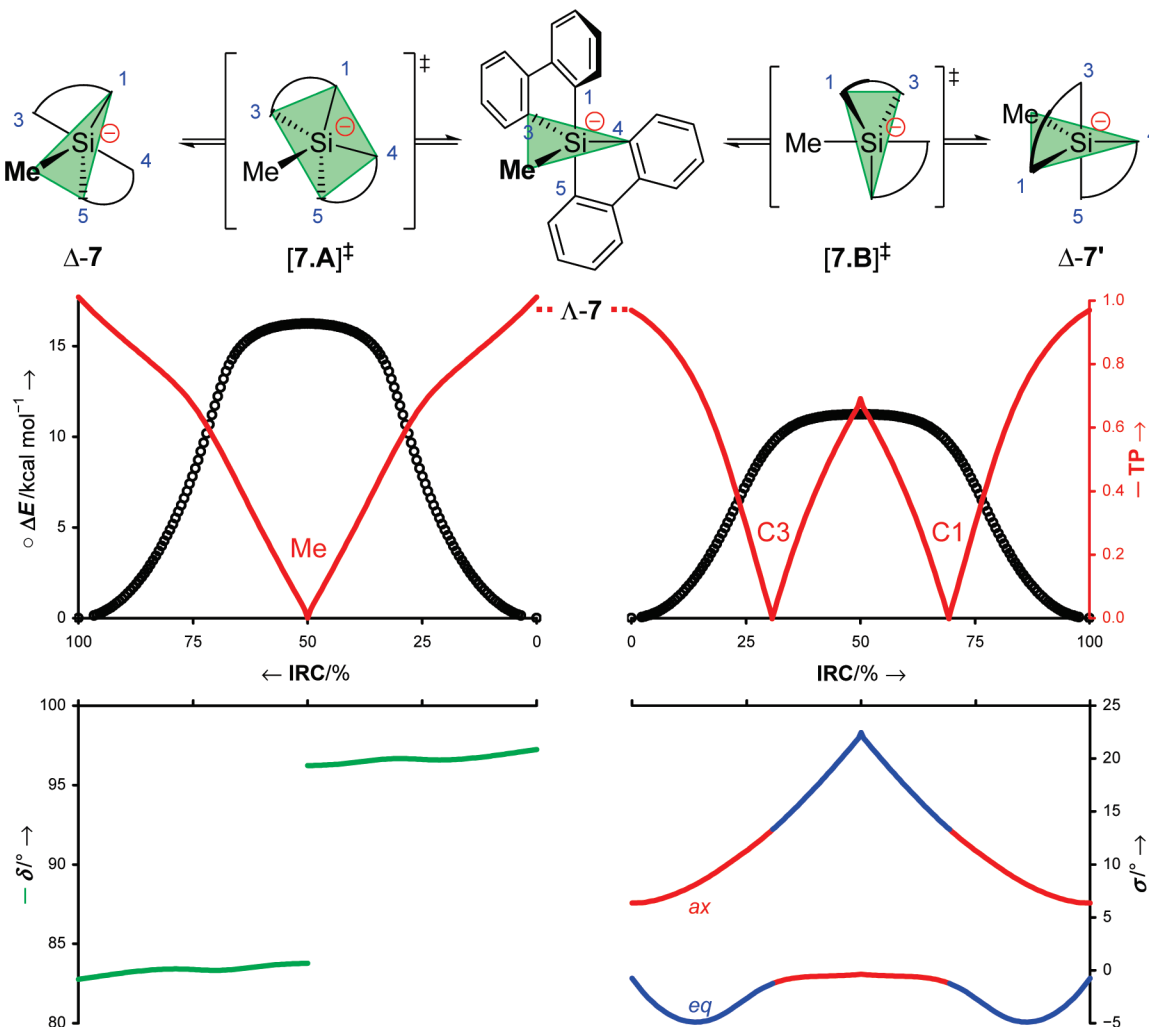
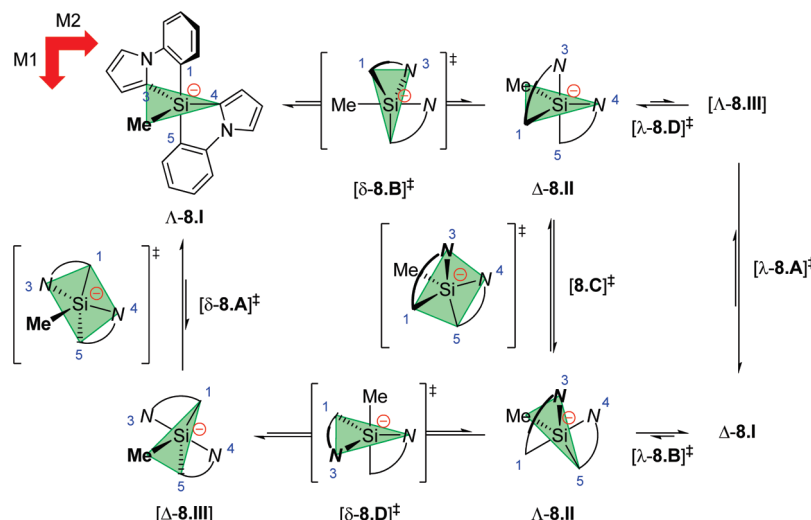


**Figure 9.** Enantiomerization of **7** via general mechanisms M1 (left) and M2 (right); for clarity, the biphenyl-2,2'-diyl groups are represented by arcs. The upper pair of graphs show the relative energy  $\Delta E$  (black) and topology parameter TP (red) along the IRCs, with pivot atom assignments. The lower pair of graphs show the corresponding dihedral angle  $\delta$  between the axial and equatorial planes (green) and the slanting angles  $\sigma_{ax}$  (red) and  $\sigma_{eq}$  (blue); discontinuities are due to the changes in atom assignment that occur at the cusps of the TP plots (see section 1.6 of the Addendum in the Supporting Information).

**Scheme 7.** Stereomutations of **8**<sup>a</sup>



<sup>a</sup> Vertical stereomutations proceed via Muetterties' mechanism M1 and horizontal ones via mechanism M2. For clarity, the phenylpyrrol-2,2'-diyl groups are represented by arcs with the N marking the pyrrole end. Prefixes  $\lambda/\delta$  designate enantiomeric pairs of transition states.

shown,  $\Delta-8.I \rightleftharpoons \Delta-8.II$  and  $[\Delta-8.III] \rightleftharpoons \Delta-8.II$ , proceed by Muetterties' mechanism M2 (double-V-shaped TP profile) and

have TBP-like transition structures  $[8.B]^\ddagger$  and  $[8.D]^\ddagger$ , respectively, with the methyl group at the axial site. The results of

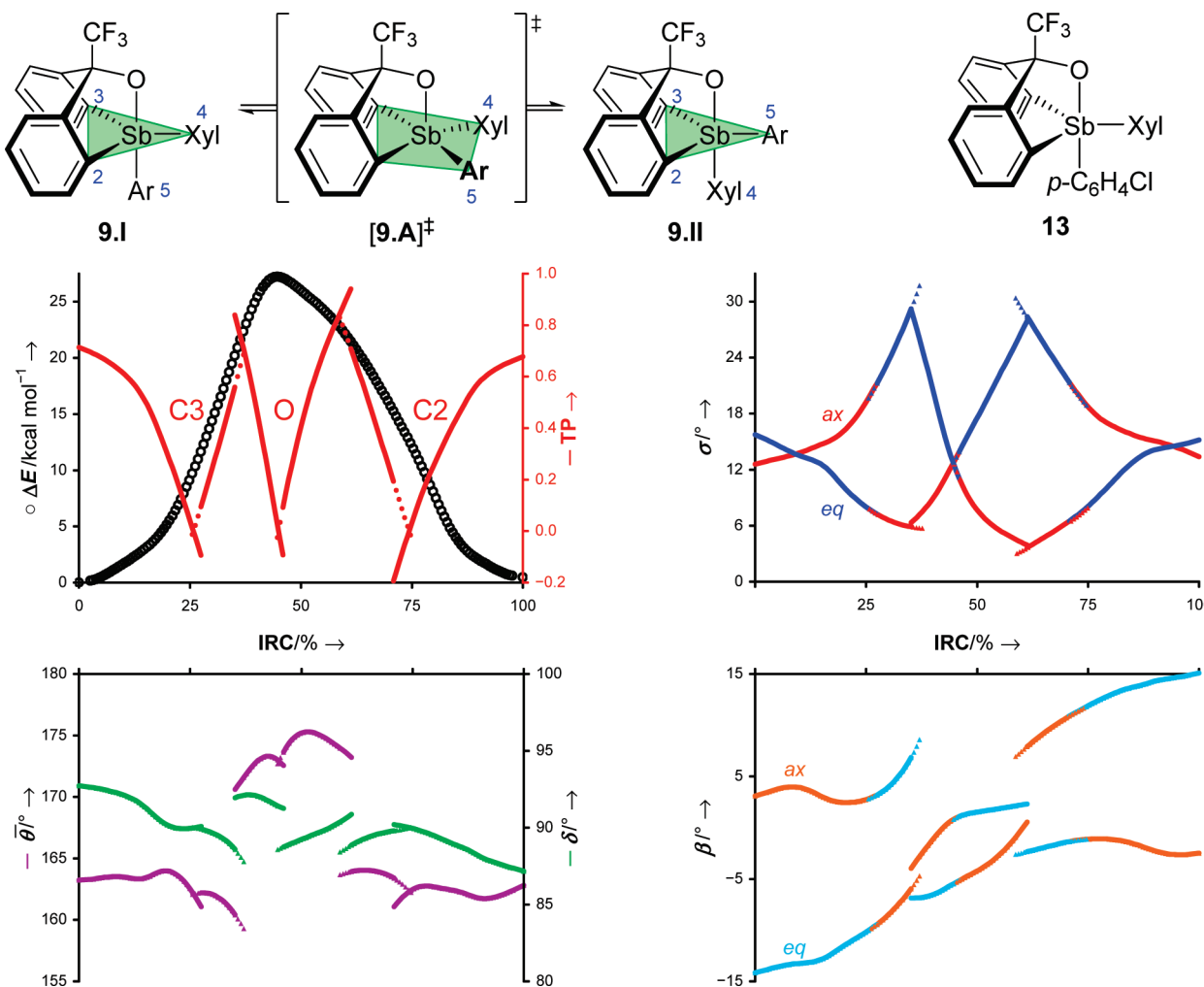


**Figure 10.** Epimerization of **9** ( $\text{Xyl} = 3,5\text{-C}_6\text{H}_3\text{Me}_2$ ,  $\text{Ar} = 4\text{-C}_6\text{H}_4\text{CF}_3$ ) via general mechanism M3. The top-left graph shows the relative energy  $\Delta E$  (black) and topology parameter TP (red) along the IRC, with pivot atom assignments. In clockwise order, the other graphs show the trends of the slanting angles  $\sigma_{\text{ax}}$  (red) and  $\sigma_{\text{eq}}$  (blue), the out-of-plane bending angles  $\beta_{\text{ax}}$  (orange) and  $\beta_{\text{eq}}$  (cyan), and the average trans angle  $\bar{\theta}$  (purple) and the *ax/eq* plane dihedral angle  $\delta$  (green). Dotted curve sections were obtained by swapping the assignments of the *ax,ax* and *eq,eq* pairs (see the text).

the reaction path analyses (see the Supporting Information) are fully analogous to those for **7**.

Having comprehensively discussed Muettterties' mechanisms M1 and M2, we now turn to molecular systems that display an M3 perturbation.

**M3: Half-Twist Axial–Equatorial Interchange.** The group of Yamamoto<sup>33</sup> recently synthesized and characterized the caged pentavalent antimony compounds **9** and **13**, both of which exist in solution as two slowly interconverting stereoisomers. For **9**, they determined a barrier of  $\Delta^{\ddagger}G_{363\text{K}} = 28.5 \text{ kcal mol}^{-1}$  by variable-temperature NMR spectroscopy. The *ax–eq* substituent interchange was suggested to take place via a “threefold TR [motion]”, which corresponds to Muettterties’ mechanism M3 in Scheme 3. Our exhaustive IRC calculations on these large systems confirmed that the stereoisomers **9.I** and **9.II** interconvert directly via a single SP-like transition structure **[9.A]<sup>‡</sup>**, as shown by the energy profile in the top-left graph of Figure 10. The same graph shows a corresponding triple-V-shaped pattern for the TP, albeit with discontinuities (see below). Evidently, three consecutive Berry motions take place, where in turn each coordinating atom of the tridentate substituent acts as the pivot, thereby distinguishing this general process from all those discussed above.

The triple-V-shaped TP pattern warrants closer scrutiny. Its two maxima, which are located on either side of the TS at  $\sim 36$

and 62% of the reaction coordinate, have nonstationary, distorted TBP geometries. These are destabilized by the electronegative oxygen atom at an *eq* site and the cage strain imposed by the rigid tridentate structure, causing the slanting angle  $\sigma_{\text{eq}}$  to approach 30° (Figure 10, top-right graph). The considerable steric crowding that occurs between the interchanging aryl substituents and the *o*-phenylene moieties of the tridentate group is reflected in large out-of-plane bending angles  $\beta_{\text{eq}}$  and  $\beta_{\text{ax}}$  for the first and last Berry motions (bottom-right graph) and in a large average trans angle  $\bar{\theta}$  of 170–175° for the middle Berry deformation (bottom-left graph). These large distortions are the cause of the discontinuities in the TP profile, as the assignment of the *ax,ax* and *eq,eq* pairs is based on the valence angles between the substituents while the TP parameter is derived from the angles between the *plane-projected* bonds. In an extreme case for a near-SP geometry in which the *ax,ax* bond pair is considerably out of plane with the pivot bond, the projected angle can become smaller than that of the *eq,eq* bond pair, which would give a negative TP value. To address this unwanted effect, we reanalyzed the affected structures with swapped *ax,ax* and *eq,eq* assignments, and the results are shown by the dotted lines in the graphs of Figure 10. With this simple modification, an uninterrupted triple-V-shaped TP profile was obtained.

We now turn to the caged oxyphosphorane **10** on which Denney and co-workers reported briefly.<sup>36</sup> They observed two

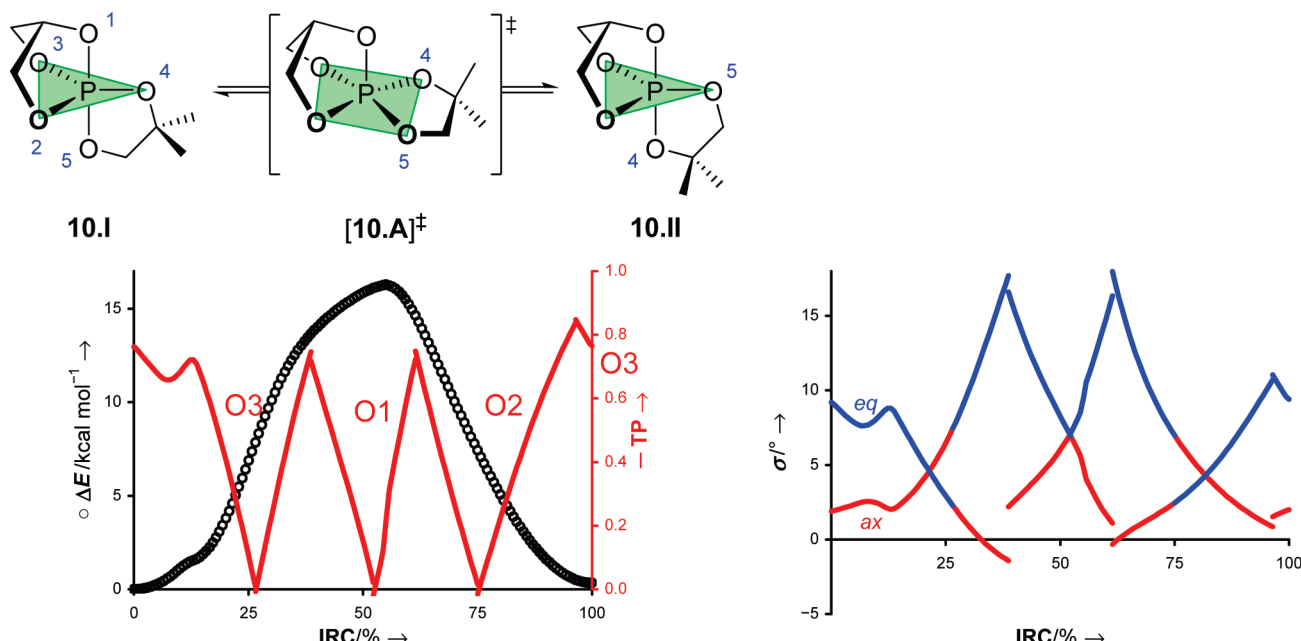


**Figure 11.** Epimerization of phosphorane **10** via general mechanism M3. The left graph shows the relative energy  $\Delta E$  (black) and topology parameter TP (red) along the IRC, with pivot atom assignments. The right graph shows the slanting angles  $\sigma_{ax}$  (red) and  $\sigma_{eq}$  (blue).

distinct  $^1\text{H}$  NMR methyl resonances in a 3:2 ratio that coalesced at  $74\text{ }^\circ\text{C}$ , which suggests the existence of two interconverting isomers with a barrier of  $\sim 19\text{ kcal mol}^{-1}$ . Our calculations corroborated this interpretation with a free energy barrier of  $\Delta_f^{\ddagger}G_{347\text{K}} = 15.6\text{ kcal mol}^{-1}$  for conversion of **10.I** into the 0.5  $\text{kcal mol}^{-1}$  less stable **10.II**. The IRC calculations showed that this single-step conversion occurs via a true half-twist stereomutation of which the transition structure **[10.A] $^{\ddagger}$**  has an SP-like geometry (Figure 11, left).<sup>43</sup> The topology parameter for this process has a triple-V-shaped pattern, implying three consecutive Berry-type motions. In contrast to **9**, this profile is uninterrupted in the case of the sterically uncongested **10** because of the modest out-of-plane bending angles  $\beta_{ax}$  and  $\beta_{eq}$  and the normal average trans angle  $\bar{\theta}$  (see the Supporting Information). Similar to the pronounced slanting angles for the enantiomerization of **7** via TS **[7.B] $^{\ddagger}$** , the geometrical constraints of the tridentate ligand of **10** cause the angle  $\sigma_{eq}$  to be large near the nonstationary TBP-like geometries at 39 and 61% of the reaction coordinate (Figure 11, right).

The last system we discuss is the closely related phosphorane **11**, which also represents a special case. The reported coalescence of the *ax* and *eq*  $\text{CF}_3$   $^{19}\text{F}$  NMR resonances<sup>36</sup> suggests a degenerate interchange. Because of the structural resemblance with **10**, the half-twist stereomutation of the dithiolate ligand that interconverts the TBP-like geometries of **11.I** and **11.I'** (Figure 12, top) is also expected to be a single-step process following general mechanism M3. However, the calculations reveal a more complex reaction profile with a very shallow minimum instead of a single TS for the permutation (see the graph in Figure 12). Because the kinetic stability of this intermediate **[11.II]** with an SP-like geometry is only 1.13  $\text{kcal mol}^{-1}$  at the B3LYP/6-311++G(2d,p) level (see the Supporting

Information), it cannot be excluded that the nature of this stationary point may change at more sophisticated levels of theory, but be that as it may, the potential energy surface surrounding **[11.II]** should remain rather flat. Nevertheless, as expected, the TP shows a triple-V-shaped pattern that is characteristic of three consecutive Berry-type motions. The behavior of **11** is unique in that the calculations show the stereomutation to be a two-step process following mechanism M3 (i.e., 1.5 consecutive Berry-type deformations per step). Formally, this behavior does not resemble any of Muettterties' mechanisms (Scheme 3) because SP minima were not considered. There are many more instances, such as for transition-metal complexes, where SP minima can have kinetic viability on the stereomutation pathway, thereby providing a means to influence the stereochemical control. We are currently investigating this area.

**Stereomutational Mechanisms and Graph Theory.** We are unaware of any experimental system that stereomutates according to general mechanism M4 or M5 (see section 1.5 of the Addendum in the Supporting Information for a forced direct enantiomerization of  $\text{PF}_5$ ). Therefore, in this section we combine the preceding results with graph theory to obtain a more general concept of stereomutational mechanisms, which is also useful for making predictions concerning M4- and M5-type substituent permutations.

Mathematically, there are 20 possible TBP isomers of a given pentavalent species, and the topological relationship of any isomer to the other 19 gives rise to a subdivision into six groups. This can be represented by a Levi–Desargues graph, shown on the left in Scheme 8,<sup>44</sup> in which each node corresponds to an isomer; the node labels identify the *ax* substituent numbers in such a manner that the *eq* numbers increase in a clockwise direction when the isomer is viewed down the first *ax* bond listed. The edges connect isomers that can be directly interconverted via a Berry-type motion; the attached labels then indicate which *ax,ax* and *eq,eq* substituent pairs are interchanged.

In cases where some of the isomers are not chemically feasible, such as those with a bidentate substituent in a bisaxial

(43) We identified an almost isoenergetic transition structure, **[10.B] $^{\ddagger}$** , that merely has a different staggered conformation of the  $\text{H}_2\text{C}-\text{CMe}_2$  bond of the bidentate substituent. Likewise, this bond is twisted out of the  $C_s$  symmetry plane in the minima **10.I** and **10.II** with inversion barriers of 1.5 and 1.2  $\text{kcal mol}^{-1}$ , respectively (see the Supporting Information).

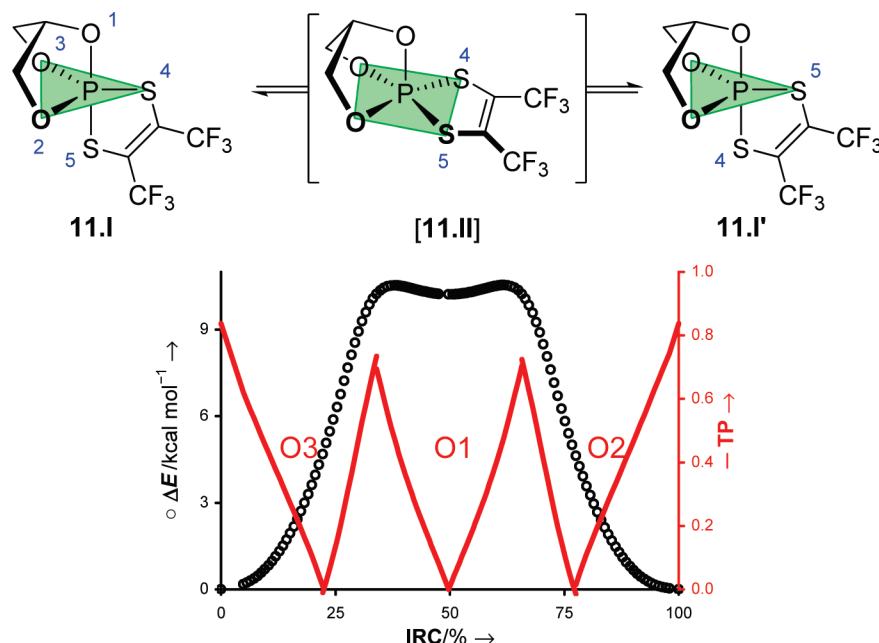
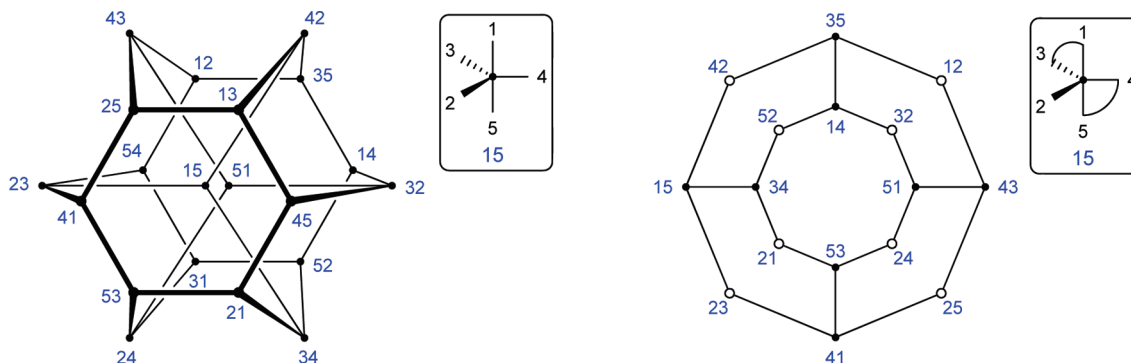


**Figure 12.** (top) Interconversion of structures and (bottom) relative energies  $\Delta E$  (black), the TP behavior (red), and indication of the pivot atoms in the stereodynamics of **11**.

**Scheme 8.** (left) Levi–Desargues Graph for BPR Interchange of TBP Isomers; (right) Subgraph for Stereomutation of Spirocyclic **7** and **8**, in Which Solid Nodes Represent Minima and Open Circles Represent TBP-Type Transition Structures (The Labeling Is Explained in the Text)



arrangement,<sup>44b,d–g</sup> the graph can be simplified by removal of such nodes.<sup>44d</sup> Other isomers may be sterically or electronically destabilized to the extent that they are no longer local minima. An example of such a simplified graph is the one for the stereomutation of the spirocyclic molecules **7** and **8** (Scheme 8, right). The open circles in this graph correspond to TBP-like transition structures having one biaryl moiety in an *eq.eq* arrangement. It should be noted that for **8**, the top and bottom halves of this graph are degenerate and that the top half corresponds to the reaction network shown in Scheme 7.

Our analyses support the notion that the Berry pseudorotation is the fundamental mechanistic pathway for interconversion of TBP-type isomers. Mechanism M2 involves a double Berry deformation involving a TBP transition structure, and mecha-

nism M3 shows a triple Berry motion in which the two intermediary TBP structures are nonstationary points on the potential energy surface. In other words, mechanisms M2 and M3 follow two and three consecutive edges, respectively, of the Levi–Desargues graph.

The threefold connectivity of each node can have interesting implications. For example, a node may serve as the TS for a two-edge M2-type interchange yet be a minimum with respect to BPR along the third edge. Such behavior has been shown computationally for  $\text{SiH}_4\text{F}^-$  and  $\text{PH}_4^+$ <sup>45</sup> and results in bifurcation of the BPR pathway. Alternatively, a node may be the M2-type TS for all three edges to afford an effective monkey saddle,<sup>46</sup> as, for example, in the cases of  $\text{SbCl}_4^-$ ,  $\text{ClF}_4^+$ , and  $\text{PH}_2(\text{CN})_3$ .<sup>47</sup>

Our results show that the Levi–Desargues graph in Scheme 8 qualitatively depicts the low-energy regions on the multidimensional potential energy surface.

(44) See refs 14a, 13a, and: (a) Dunitz, J. D.; Prelog, V. *Angew. Chem., Int. Ed. Engl.* **1968**, *7*, 725–726. (b) Lauterbur, P. C.; Ramirez, F. *J. Am. Chem. Soc.* **1968**, *90*, 6722–6726. (c) Mislow, K. *Acc. Chem. Res.* **1970**, *3*, 321–331. (d) Hellwinkel, D.; Lindner, W.; Schmidt, W. *Chem. Ber.* **1979**, *112*, 281–291. (e) Kojima, S.; Kajiyama, K.; Nakamoto, M.; Matsukawa, S.; Akiba, K.-y. *Eur. J. Org. Chem.* **2006**, 218–234. (f) Jiang, X.-D.; Matsukawa, S.; Yamamichi, H.; Kakuda, K.-i.; Kojima, S.; Yamamoto, Y. *Eur. J. Org. Chem.* **2008**, 1392–1405. (g) Kojima, S.; Nakamoto, M.; Akiba, K.-y. *Eur. J. Org. Chem.* **2008**, 1715–1722.

(45) (a) Windus, T. L.; Gordon, M. S.; Davis, L. P.; Burggraf, L. W. *J. Am. Chem. Soc.* **1994**, *116*, 3568–3579, and references therein. (b) Yanai, T.; Taketsugu, T.; Hirao, K. *J. Chem. Phys.* **1997**, *107*, 1137–1146.

(46) Mezey, P. *Potential Energy Hypersurfaces*; Elsevier: New York, 1987.

(47) (a) Mauksch, M.; Schleyer, P. v. R. *Inorg. Chem.* **2001**, *40*, 1756–1769. (b) Sadasivam, D. V.; Karney, W. L.; Tamas, G.; Couzijn, E. P. A.; Birney, D. M. Manuscript in preparation.

dimensional potential energy surface for the M1, M2, and M3 stereomutations of pentavalent compounds. However, the mechanisms M4 and M5 as proposed by Muetterties<sup>14</sup> do not follow the edges of this graph; the “anti-Berry” permutation via M4 would correspond to a direct connection of, for example, node 15 with node 24, 32, or 43, whereas M5 would directly connect opposite nodes (e.g., 15 and 51 in Scheme 8). We suggest that such permutations instead take place via the graph edges, thus requiring four and five consecutive Berry-type motions, respectively. Only the initial and final TBP geometries should be minima, making the design of such systems highly challenging.

## Conclusions

The stereomutations of pentavalent compounds are readily characterized by full parametrization of the five-coordinate geometries along the intrinsic reaction coordinates. The trends in the geometry parameters give a straightforward interpretation of the general interchange mechanism as well as of any constraints imposed by the substituents. As a result of the use of internal coordinates, this approach is unaffected by any overall molecular reorientation, much in contrast to interpretations of both the permutational scheme and the transition vector for stereomutation. Thus, we have been able to demonstrate irrefutably that the turnstile rotation (TR) is equivalent to the Berry pseudorotation (BPR). The truly alternative cyclic-permutation (M2) and half-turn (M3) mechanisms involve two and three consecutive Berry-type motions, respectively. These general mechanisms cannot be distinguished from BPR by correlation of X-ray structures because they differ only in regard to their energy profiles.

The cyclic permutation (M2) resembles the 120° rotational motion of a mechanical three-arm turnstile gate, whereas TR describes only a 60° rotation. Mechanism M2 is the most viable alternative to the more prominent BPR, so reassigning the name “turnstile rotation” to M2 would reconcile most of the former literature with the current findings. This is also consistent with the IUPAC description (but not the visualization<sup>11</sup>) of TR and with the corresponding stereomutational mechanism for octahedral compounds. Thus, our approach resolves the existing ambiguities surrounding stereomutation of pentavalent compounds and inspires the design of systems that feature yet unobserved general mechanisms.

## Computational Section

DFT calculations were performed with Gaussian 03<sup>29</sup> employing an ultrafine integration grid and tight SCF convergence criteria. Fluorophosphorane **1**, chlorofluorophosphorane **3**, and PH<sub>5</sub> were treated at the B3LYP/6-311++G(2d,p) level of theory, larger main-group compounds at the B3LYP/6-31G(d) level [LanL2DZ(d) with Cartesian d functions for antimony], and transition-metal complexes **4–6** at the B3PW91/SDD(d) level. SDD(d) is a custom Cartesian basis set consisting of the Stuttgart/Dresden basis set and effective core potential<sup>48</sup> for the metal and the Dunning 95 full double- $\xi$  basis set<sup>49</sup> with an additional d polarization function for the other elements. For optimizations, the geometry DIIS algorithm<sup>50</sup> was applied in combination with tight geometry convergence criteria (very tight for **1**, **3**, and PH<sub>5</sub>). Frequency calculations were

(48) Dolg, M. In *Modern Methods and Algorithms of Quantum Chemistry*; Grotrendorst, J., Ed.; John von Neumann Institute for Computing: Jülich, Germany, 2000; Vol. 1, pp 479–508.

performed to confirm the nature of each stationary point and to obtain the thermochemical corrections using the customary scaling factors of 0.9877 for B3LYP/6-311++G(2d,p)<sup>51</sup> and 0.9804 for B3LYP/6-31G(d).<sup>52</sup> Subsequent single-point energies were calculated for the larger main-group compounds with the 6-311++G(2d,p) basis set (LanL08d<sup>53</sup> with Cartesian d functions for antimony) and for the transition-metal complexes with the SDB-cc-pVTZ basis set.<sup>30</sup> For **4**, the calculated activation energy was determined according to  $E_a = \Delta^\ddagger H + RT$ .<sup>54</sup>

IRC calculations were performed with the same settings as for the optimizations. In general, the most nearly complete IRC pathways were obtained by following the path in Cartesian coordinates without mass weighting. In cases of problematic geometry convergence, the original TS geometry was supplied in Z-matrix coordinates. IRC step sizes were chosen to give a sufficient number of intermediate structures (typically >40) on either side of the TS in order to accurately track the geometrical changes. The IRC calculations for stiborane **9** were performed with Gaussian 09<sup>55</sup> using the Hessian-based predictor-corrector (HPC) integrator<sup>56</sup> with tight convergence and Hessian reevaluation at each predictor step; the small-gradient stopping criterion was turned off with IOp(1/108=−1). The intermediate geometries of each IRC calculation were extracted to a multistucture XYZ file, which served as input for the geometry analysis program. To estimate the position of each minimum on the reaction path, up to half of the intermediate energies were extrapolated using a third-degree polynomial function of the squared reaction coordinate. Further details concerning the IRC pathways and graphs of the analysis results for all of the investigated systems are provided in the Supporting Information.

Animations of the stereomutational IRC pathways (see footnote b of Table 2) were created for selected molecules using the 3D molecule viewer Jmol.<sup>57</sup>

**Acknowledgment.** This work was supported by The Netherlands Organisation for Scientific Research, Chemical Sciences (NWO-CW). We acknowledge SARA Computing and Networking Services for computer time and Profs. Y. Yamamoto and D. M. Birney for constructive discussions. E.P.A.C. is grateful for the support of Prof. P. Chen at ETH Zürich.

**Supporting Information Available:** Addendum; complete refs 29 and 55; comparison of X-ray crystal structures with optimized geometries; optimized coordinates, energies, and thermochemical corrections; details of the IRC calculations; and graphs of all geometry analyses. This material is available free of charge via the Internet at <http://pubs.acs.org>.

JA105306S

- (49) Dunning, T. H., Jr.; Hay, P. J. In *Modern Theoretical Chemistry*; Schaefer, H. F., III, Ed.; Plenum: New York, 1976; Vol. 3, pp 1–28.
- (50) Farkas, Ö.; Schlegel, H. B. *J. Chem. Phys.* **1999**, *111*, 10806–10814.
- (51) Andersson, M. P.; Uvdal, P. *J. Phys. Chem. A* **2005**, *109*, 2937–2941.
- (52) (a) Foresman, J. B.; Frisch, A. *Exploring Chemistry with Electronic Structure Methods*, 2nd ed.; Gaussian, Inc.: Pittsburgh, PA, 1996. (b) Wong, M. W. *Chem. Phys. Lett.* **1996**, *256*, 391–399.
- (53) (a) Roy, L. E.; Hay, P. J.; Martin, R. L. *J. Chem. Theory Comput.* **2008**, *4*, 1029–1031. (b) Check, C. E.; Faust, T. O.; Bailey, J. M.; Wright, B. J.; Gilbert, T. M.; Sunderlin, L. S. *J. Phys. Chem. A* **2001**, *105*, 8111–8116.
- (54) Muller, P. *Pure Appl. Chem.* **1994**, *66*, 1077–1184.
- (55) Frisch, M. J.; et al. *Gaussian 09*, revision A.02; Gaussian, Inc., Wallingford, CT, 2009.
- (56) Hratchian, H. P.; Schlegel, H. B. *J. Chem. Phys.* **2004**, *120*, 9918–9924.
- (57) See: <http://jmol.sourceforge.net/>.